JOURNAL OF SPACECRAFT AND ROCKETS
Vol. 44, No. 1, January–February 2007

CFD Contribution to the Aerodynamic Data Set of the Vega Launcher

P. Catalano,* M. Marini,† and A. Nicoli‡
CIRA Italian Aerospace Research Center, 81043 Capua, Italy
and
A. Pizzicaroli§
AVIO, 00034 Colleferro, Italy

DOI: 10.2514/1.23534

This paper presents the CFD activities performed to simulate the subsonic, transonic, and supersonic flow around the four-stage configuration of the Vega launcher in motor-on conditions. Numerical simulations, complementary to experimental test campaigns, have been performed covering a range of Mach numbers from 0.50 to 3.02, two angles of attack, and three Reynolds numbers. The flight and the wind tunnel configurations of the launcher have been considered. The Reynolds-averaged formulation of the Navier–Stokes equations has been adopted. The engine conditions have been reproduced by a boundary condition that allows to impose density, pressure, and momentum at the nozzle exit section. A globally satisfactory agreement between numerical simulations and experiments has been achieved over a wide range of flow regimes, in terms of both local and global properties, and the main flow structures have been well predicted. The paper shows the key role that CFD has played in supporting wind tunnel activities, and in providing data for the determination of extrapolation-to-flight procedure.

Nomenclature

C_A	=	global axial force coefficient
C_a	=	local axial force coefficient
C_D	=	global drag coefficient
C_L	=	global lift coefficient
C_M	=	global pitching moment coefficient
C_m	=	local pitching moment coefficient
C_N	=	global normal force coefficient
C_n	=	local normal force coefficient
C_P	=	pressure coefficient
D	=	maximum diameter of the launcher
h	=	grid spacing
L	=	length, grid level
M	=	Mach number
r	=	radial coordinate
Re	=	Reynolds number
S	=	surface
X, x	=	longitudinal axis
X_{CP}	=	center of pressure
y^+	=	viscous coordinate
Z, z	=	vertical axis
α	=	angle of attack
γ	=	specific heats ratio
κ	=	turbulent kinetic energy
ω	=	specific dissipation rate

Subscripts

Base	=	base
fin	=	final (last iteration of a numerical simulation)
FL	=	flight
INT	=	intermediate
REF	=	reference
WT	=	wind tunnel

I. Introduction

IN the framework of the European Space Agency (ESA) project Vega, CIRA has been charged by Italian industry AVIO to study the aerodynamics of the launcher from the subsonic to the hypersonic regime, and to produce a detailed aerodynamic data set. The final goal of the activity was the evaluation of the global aerodynamic coefficients along the ascent path of the launcher. Wind tunnel test campaigns have been conducted in several facilities to cover the flow regimes experienced by the vector. A procedure to correct the measured aerodynamic coefficients to the actual flight conditions was needed. The focus of the paper is placed on the CFD simulations performed to better drive the experimental test campaigns and to support the extrapolation procedure. The flight and wind tunnel configurations of the launcher, two angles of attack, and three Reynolds numbers have been considered. The flight configuration (Fig. 1) is equipped with a propulsive nozzle where the exit flow conditions of the P80FW engine of the Vega launcher have been imposed. The wind tunnel configurations are 1:30 scaled and are equipped with a device to model the jet exiting from an annular engine. The Reynolds-averaged formulation of the Navier–Stokes equations has been adopted. This approach results to be not very computationally expensive and is supposed to provide an accuracy sufficient to the goals of the project. Drawbacks were expected in the prediction of the base flow. The effect of this issue on the definition of the laws to extrapolate the aerodynamic coefficients to the flight conditions has been addressed by properly analyzing the experimental and numerical data. The final result, in the form of distributions of the normal and axial force coefficient as function of Mach and Reynolds numbers, has been achieved. All the numerical simulations have been performed before the wind tunnel test campaigns, and the flow specification has been derived by the atmospheric conditions evaluated along the trajectory of the

Presented as Paper 4964 at the 23rd AIAA Applied Aerodynamics Conference, Toronto, 6–9 June 2005; received 28 February 2006; revision received 3 May 2006; accepted for publication 17 May 2006.

*Research Engineer, Computational Fluid Dynamics Laboratory.
†Research Engineer, Ph.D., Aerothermodynamics and Space Propulsion Laboratory.
‡Research Engineer, Transonic Wind Tunnel Laboratory. Member AIAA.
§Vega Aerodynamics Chief Engineer, Technical Direction—Mechanical Design.

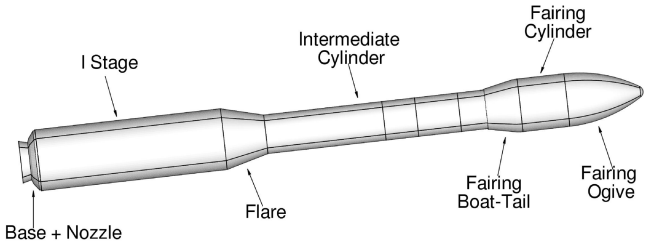

Fig. 1 Flight configuration.

launcher. The numerical results obtained in the subsonic, transonic, and supersonic flow regimes up to Mach number 3.0 are presented, compared with the experimental data, and critically discussed.

II. Experiments

Experimental test campaigns have been conducted, under CIRA supervision, in the FOI (Swedish Defence Research Agency) T1500 wind tunnel for the subsonic/transonic flow conditions ($0.5 \leq M \leq 1.2$), and in the DNW (German–Dutch Wind Tunnel foundation) SST for the supersonic regime ($1.58 \leq M \leq 3.96$). Pressure measurements, global aerodynamic forces and moments, and flow visualizations have been carried out.

The 1:30-scaled model of the launcher was equipped with a cold air plume simulator with an annular nozzle to reproduce the effect of the jet plume on the base drag and pressure. The design of the plume simulator was based on the "component" method [1].

The global aerodynamic coefficients were measured by a six-component balance up to $\alpha = 10$ deg. The model was instrumented with 48 pressure taps along a generatrix line. Four taps along a generatrix line plus other six taps to form a semiring were placed on the base. The pressures were acquired by two electronically scanned transducers (ESP) placed inside the model in the payload region and calibrated before each run. To map the pressure field around the overall launcher, the pressures were acquired along seven different generatrix lines, equally spaced of 30 deg in the azimuthal direction between the lee and the wind side. The uncertainty of the measured C_P is reported in the Table 1. This was estimated from the uncertainties of the wind tunnel test conditions and the uncertainties of the pressure instrumentation used, following the error propagation methodology [2]. Oil flow visualizations with titan bioxide were performed at $M = 0.90$, 1.20, 1.58, 2.01, and 3.0 at $\alpha = 2$ deg and/or $\alpha = 5$ deg.

III. Numerical Method

The CIRA Zonal Euler Navier–Stokes (ZEN) flow simulation system has been applied for all the numerical computations. This system is integrated with commercial pre- and postprocessors and consists of a grid generator, a flow solver, and a set of utilities for the visualization of the convergence data. The ICEM-CFD software package is used to create or modify a CAD geometry, and to generate the topology and the computational mesh. An interface, embedded in ICEM-CFD, allows to obtain grids in a format directly usable for the solver, and to set the boundary conditions and the visualization data. The interface has been developed by ICEM, under technical specifications provided by CIRA, and deeply verified on several applications. The in-house developed code, ZEN, is the flow solver and represents the core of the system. ZEN is a very robust, efficient, and well-assessed multiblock computational tool for the analysis of complex configurations in the subsonic, transonic, and supersonic regimes [3]. The governing equations are discretized by means of a finite volume cell-centered formulation. A central differencing scheme with blended self-adaptive second- and fourth-order artificial dissipation is used. The solution procedure is based on a pseudo-time-marching concept. The multigrid scheme is used to accelerate the convergence of the solution, and performs relaxations, by using the Runge–Kutta algorithm with local time stepping and residual averaging, on different grid levels. Implicit residual smoothing, enthalpy damping, and local block refinement are other numerical techniques employed. A preconditioning method for low-speed flows is also implemented. The code is parallelized by using different message passing softwares like message passing interface (MPI), parallel virtual machine (PVM), and open message passing (OMP). The turbulence equations are uncoupled by the Reynolds-averaged Navier–Stokes (RANS) equations and solved only on the finest grid level of a multigrid cycle. Algebraic, one-equation, two-equation [4], and nonlinear eddy viscosity [5] turbulence models are available. The κ–ω model proposed by Kok [6] has been applied for all the simulations presented in the paper. A time-accurate version of the flow solver has been developed and is currently under validation [7].

Table 1 Uncertainty of the measured pressure coefficients evaluated at $C_P = 0$

Mach	C_P uncertainty
0.50	±0.008
0.80	±0.003
0.85	±0.003
0.90	±0.003
0.95	±0.003
1.07	±0.002
1.20	±0.002
1.58	±0.003
1.72	±0.002
2.01	±0.003
2.50	±0.003
3.00	±0.006
3.96	±0.039

IV. Grid Generation

Structured multiblock grids for the flight configuration (Fig. 1) and 1:30-scaled model of the Vega launcher have been generated by means of a software package ICEM-CFD. The mesh for the full-scale configuration in the subsonic and transonic flow regimes employs a C-O topology with the farfield boundaries placed at about five body lengths. The total number of points is about 2.81 million and is the result of a compromise between the requirements dictated by the flight Reynolds number and grid details, and a reasonable CPU time. Figure 2 shows the block decomposition and an enlargement of the mesh in the base and nozzle region. Other two meshes have been generated for the supersonic simulations. The external boundaries have been adapted to the flow regime: the inflow surface has been determined by considering the standoff distance and a suitable shock shape given by the Billig correlation formulas [8], whereas the outflow plane has been placed at about three body lengths for $M = 2.01$ and one body length for $M = 3.02$. The total number of points is decreased to 2.42 million for $M = 2.01$ and 1.47 million for $M = 3.02$. The block decomposition and an enlargement of the mesh in the zone of base and nozzle are presented in Fig. 3.

The model used in the wind tunnel tests is 1:30 scaled with respect to the flight configuration and is equipped with a device to simulate the plume exiting from the engine. Two different configurations of the plume simulator system, shown in Fig. 4, have been designed by

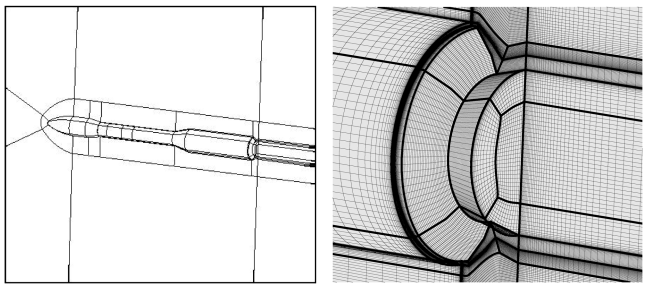

a) Domain decomposition **b) Base and nozzle region**

Fig. 2 Grid for flight configuration in subsonic and transonic flow regime.

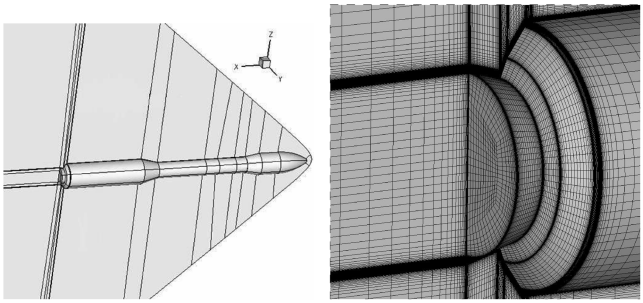

a) Domain decomposition b) Base and nozzle region

Fig. 3 Grid for flight configuration in supersonic flow regime.

FOI: one "shaped" for the subsonic and transonic regimes, and another "stepped" for the supersonic tests. The grids generated for the wind tunnel configurations have been obtained by scaling the meshes generated for the full-scale launcher, and by changing the topology in the region of the annular nozzle and sting. Details of the grids used to reproduce the experimental tests are shown in Fig. 5. It is worth noting that the proper geometrical definition of the plume simulator system has required additional blocking and wall stretching, thus in general increasing the total number of points (i.e., at $M = 3.02$ from 1.47 to 1.89 million).

The values of the viscous turbulent coordinate of the wall-adjacent layer of cells have been analyzed. The transonic simulations in flight conditions present the highest Reynolds numbers, thus the worst situation. The values are between 4 and 6 along all the launcher with exception of the rear part of the I stage, where there are regions with y^+ about 9. For the subsonic and transonic simulations around the wind tunnel configuration, y^+ ranges between 1 and 2 along all the configuration. The highest values (about 5) are always obtained on the rear end of the I stage. The situation is quite good for the supersonic regime. The y^+ is less than 1 in the front part of the launcher and remains always lower than 4. However, the turbulence model employed (κ–ω model proposed by Kok [6]) has the advantage to not have a direct dependence of the eddy viscosity on the distance from a solid surface, and this should allow to relax the requirements on y^+. The same turbulence model has been used to perform simulations of high Reynolds number flows by employing no-slip boundary conditions and a wall function formulation [9]. The wall-integrated results have shown, in terms of pressure, friction and global aerodynamic coefficients, a satisfactory accuracy provided that y^+ does not exceed 10.

Table 2 Effect of grid resolution in the transonic regime ($M = 0.95$, $\alpha = 2$ deg)

Grid level	No. of cells	C_N	C_A	C_M	X_{CP}/D
L_1	41,376	1.2478	0.7314	1.5402	1.2349
L_2	331,008	0.9884	1.0043	0.9410	0.9525
L_3	2,648,064	1.0000	1.0000	1.0000	1.0000

Table 3 Effect of grid resolution in the supersonic regime ($M = 3.02$, $\alpha = 2$ deg)

Grid level	No. of cells	C_N	C_A	C_M	X_{CP}/D
L_2	160,752	1.0260	0.9937	1.0426	1.0163
$L_{2.5}$	735,392	1.0028	0.9997	1.0118	1.0090
L_3	1,286,016	1.0000	1.0000	1.0000	1.0000

A. Effect of Grid Resolution

The effect of the grid resolution on computed results has been analyzed for the flight configuration in motor-on conditions in transonic ($M = 0.95$, $\alpha = 2$ deg), and supersonic ($M = 3.02$, $\alpha = 2$ deg) regimes. Tables 2 and 3 report the aerodynamic coefficients C_N, C_A, C_M, and the normalized center of pressure X_{CP}/D as a function of the grid resolution, all the values having been

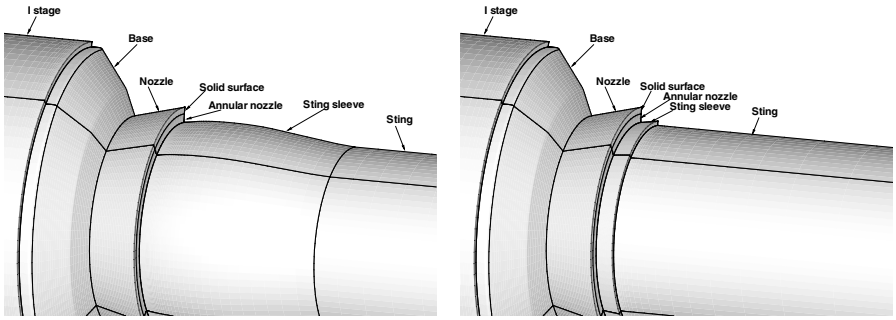

a) Subsonic/Transonic b) Supersonic

Fig. 4 Wind tunnel configuration.

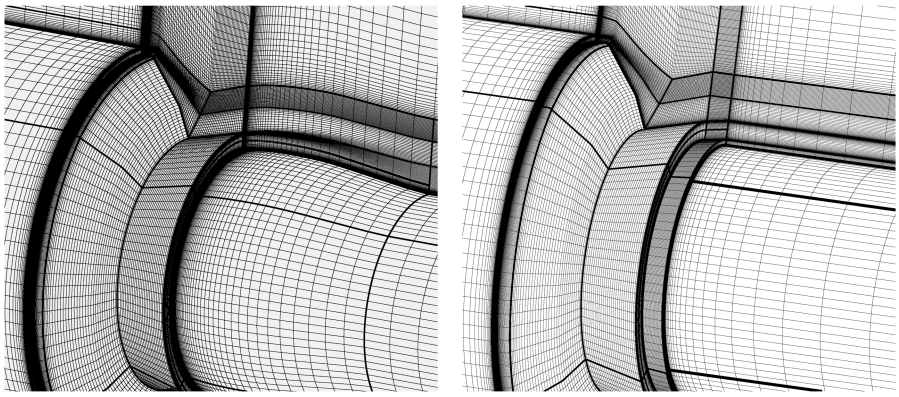

a) Subsonic/Transonic b) Supersonic

Fig. 5 Grid for wind tunnel configuration.

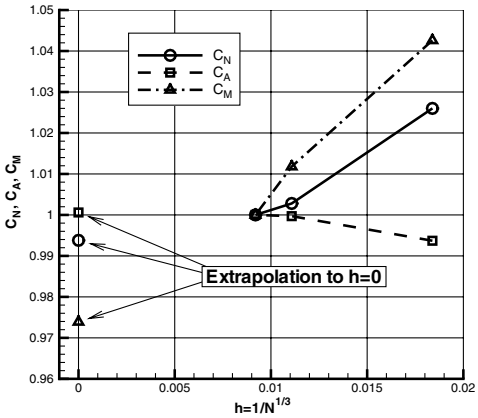

Fig. 6 Grid resolution effect in supersonic regime.

normalized to the finest grid level (L_3). The coarse grid (L_1) results for the transonic case (Table 2) have been obtained with laminar flow assumption and motor-off conditions (a strategy used to initialize the complex base flow structure), and then have to be considered only as reference values. The percentage variation between the results of the fine (L_3) and medium (L_2) grid levels is 1.17% for the normal force, −0.43% for the axial force, 6.27% for the pitching moment coefficient, and 4.98% for the position of center of pressure. Concerning the supersonic case (Table 3), the coarse level of the grid (L_1) was not adequate to capture the quite strong bow shock wave around the launcher's nose. An intermediate grid ($L_{2.5}$) between the medium (L_2) and the fine (L_3) level of the grid has been then generated to demonstrate the grid-independence of the results. For each elementary edge an intermediate number of points between those of L_2 and L_3 levels has been selected, with the spacing law scaled accordingly. Figure 6 shows the aerodynamic coefficients as a function of the parameter $h = 1/N^{1/3}$, where N is the number of cells of a grid level, this number representing the grid resolution (the accuracy of the grid increasing from right to left). The percentage variation between the result obtained on the fine (L_3) and intermediate ($L_{2.5}$) grid levels is −0.28% for the normal, 0.03% for the axial force coefficients, −1.17% for the pitching moment, and −0.90% for the position of the center of pressure. The level of convergence of the solution can be estimated by using the Richardson extrapolation method [10] applied to functionals such as the global aerodynamic coefficients. The values of C_N, C_A, and C_M have been extrapolated to zero grid spacing ($h = 0$) assuming the actual grid refinement ratio and a second order of accuracy. The discretization error of the CFD data has been evaluated looking at the difference between the quantitative results obtained on the fine grid level and the values extrapolated at $h = 0$ (Table 4). The error is of order of magnitude 10^{-4} for both C_N and C_A, and larger for C_M (it is to be noted that the pitching moment coefficient is computed with respect to the nose-tip).

Table 4 Discretization error

Flow regime	C_N	C_A	C_M
Transonic	0.0003	0.0005	0.0057
Supersonic	0.0007	0.0002	0.0099

It is possible to affirm that, in the frame of the physical and numerical modeling adopted in the present analysis, the computational grids employed in the simulations in subsonic, transonic, and supersonic regimes provide grid-independent results in terms of global aerodynamic coefficients.

B. Convergence of the Numerical Solutions

The numerical simulations have been performed by employing a three-level strategy. The block-faces of the computational mesh representing the engine have been considered as solid surfaces on the coarse and medium grid levels and as fluid surfaces on the fine level. Then density, pressure, and momentum have been taken from freestream to the values reproducing the flow conditions at the exit of the engine in several steps. Considering the part of simulations with the actual engine-on conditions applied, the residual of the density equation has decreased of about two orders of magnitude in subsonic, between two and three in transonic, and more than three in the supersonic flow regime.

The pressure and friction coefficients have been integrated on the lateral surface of the launcher which is proportional to πDL. The surface used to scale the force and moment coefficients is $\pi D^2/4$. The ratio between the integration and reference surfaces is therefore proportional to $4L/D$, a value of about 40 for the Vega four-stage configuration. Based on this consideration and on the fact that an accuracy of order of magnitude of the drag-count can be expected in a CFD simulation, a variation of less than 10 drag-counts was decided to be adequate for the convergence of the numerical solutions.

This criterion has not been satisfied in the subsonic regime where the drag coefficient has shown oscillations of about 2.5%. This unsteadiness was essentially attributed to the pressure distribution on the base as confirmed by comparison with the experimental results presented in the following sections.

The convergence of lift, drag, and pitching moment coefficients in the last 10,000 iterations is shown in Fig. 7 for the transonic flow regime. The aerodynamic coefficients are referred to the values obtained at the end of the numerical simulations. The line representing the adopted criterion is reported in bold. The C_L changes of less than 10^{-3}, and C_M less than 10^{-2}. The criterion is fulfilled earlier at $\alpha = 5.0$ deg than at $\alpha = 2.0$ deg.

The situation is better in the supersonic regime, in which a variation of 0.05% for the C_D, 0.1% for the C_L, and 0.1% for the C_M have been generally obtained. This means that the C_D is converged to the drag-count in the supersonic simulations.

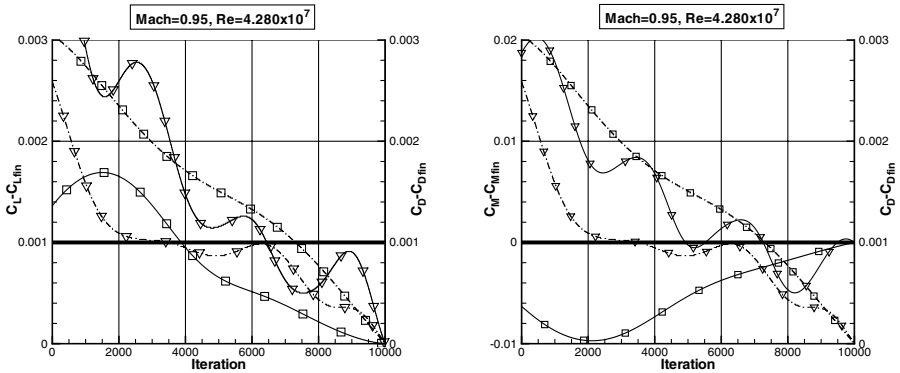

a) Lift and drag coeffcient: (solid line) C_L, (dashed-dotted line) C_D

b) Pitching moment and drag coefficient: (solid line) C_M, (dashed-dotted line) C_D

Fig. 7 Convergence of the aerodynamic coefficients in the transonic flow regime: □ $\alpha = 2.0$ deg, ▽ $\alpha = 5.0$ deg.

V. Motor-on and Plume Simulator Conditions

The flow conditions of the P80FW engine of the Vega launcher provided by AVIO have been simulated by imposing density, momentum, and pressure at the nozzle exit plane in the hypothesis of ideal gas assumption ($\gamma = \text{constant} = 1.4$). The mass flow and the ratio between the jet and the freestream static pressure have been exactly duplicated, whereas the Mach number and the temperature of the jet have been slightly under- and overestimated, respectively.

The geometric definition of the plume simulator system and external sting have been provided by FOI. Two different configurations of the plume simulator system, shown in Fig. 4, have been designed: one shaped for the subsonic and transonic regimes, and another stepped for the supersonic tests. CFD results, achieved during the first phase of the project, have been very useful to analyze the differences between the two configurations. Originally, all the tests were scheduled on the model equipped with the stepped sting, whereas the design of the second configuration, for the subsonic and transonic flow regimes, was modified following the results of a numerical sensitivity study [11]. The operation conditions of the plume simulator system, in terms of Mach number, pressure, temperature, and exit angle, have been provided as a function of the radial coordinate of the model. Numerically averaged values, always in terms of density, momentum, and pressure, have been imposed at the annular ring representing the nozzle exit. The jet angle has been taken into account by properly setting the components of the momentum.

VI. Results and Discussion

RANS simulations have been performed to study the aerodynamics of the Vega launcher in the subsonic, transonic, and supersonic flow regimes. Two angles of attack, and the wind tunnel, actual flight, and an intermediate Reynolds number determined as

$$\log_{10}\left(\frac{1}{\sqrt{Re_{\text{INT}}}}\right) = \frac{1}{2}\left[\log_{10}\left(\frac{1}{\sqrt{Re_{\text{WT}}}}\right) + \log_{10}\left(\frac{1}{\sqrt{Re_{\text{FL}}}}\right)\right] \quad (1)$$

have been taken into consideration. The 1:30-scaled wind tunnel model with the plume simulator and the sting, and the flight configuration have been considered.

Numerical sensitivity studies [11] were conducted in the first phase of the project. The grid independence of the CFD solutions was verified and the simulation techniques of the jet plume assessed. This latter point had a deep impact on the project. In fact, the design of the plume simulator for the subsonic and transonic flow regimes was modified following the results of these analyses.

The complete set [12] of simulations, as reported in Table 5, was performed before the execution of the wind tunnel campaigns. Important and detailed information on the characteristics and topology of the flow has been obtained. The aerodynamic data package has been then defined through comparison and cross-verification with the experimental data. Trends of the force and moment coefficients with the Reynolds number have been estimated.

A. Subsonic Flow Regime

In the subsonic flow regime, the wind tunnel configuration has been considered at Mach number 0.50, at $\alpha = 2$ and 5 deg. A comparison between the computed and measured pressure coefficients on the lee and wind side of the launcher model is reported in Fig. 8 for the case $\alpha = 5$ deg. The agreement is excellent over all the launcher's length except on the base. This could be expected because the prediction of the base flow, due to its intrinsic unsteady characteristics, is really critical. This has been confirmed also by the experiments. Oscillations, of order of magnitude $\pm 0.7\%$, in the measurements of the axial force coefficient were noted [13]. These oscillations were induced by fluctuations of the base pressure probably due to the interaction between the supersonic jet plume and the subsonic external flow. The unsteadiness has been filtered by the hardware of the instrumentation used on the base of the model and is not visible in the measured pressure coefficients. In the subsonic flow regime most of the C_A is due to the base [14]. Therefore, an underestimation in the prediction of the base pressure distribution is expected to reflect in a significant overprediction of the global C_A.

B. Transonic Flow Regime

In the transonic flow regime, simulations have been performed at Mach number 0.95 and 1.20, at $\alpha = 2$ and 5 deg. The Reynolds number effect has been studied at Mach 0.95 by analyzing the 1:30-scaled model with the plume simulator and the sting at the wind tunnel Reynolds number, and the full-scale configuration in motor-on conditions at the intermediate and flight Reynolds numbers. Only wind tunnel conditions have been considered at Mach 1.20.

Pressure distributions predicted at $M = 0.95$ and $\alpha = 2$ deg on the lee and wind side of the launcher are reported in Fig. 9. The numerical results compare very well with the experimental data over all the launcher, with the exception of the boat-tail region where some little differences can be noted. In this zone also the influence of the Reynolds number becomes appreciable. This is due to the fact that a flow separation occurs on the boat-tail region at both $\alpha = 2$ and 5 deg, as can be clearly seen in Fig. 10 where, at $\alpha = 5$ deg, the pressure map distribution and a comparison between the numerical (skin friction lines) and experimental (oil flow visualization) surface flow patterns are shown (a lateral view of the launcher is reported). A strong compression is present between the ogive and the faring, and a shock-induced separation occurs at the junction between the fairing cylinder and the boat-tail, as indicated in Fig. 10. A saddle point is also visible on the intermediate cylinder (lateral view shown in

Table 5 CFD test matrix

Mach	Reynolds	α	Configuration	Propulsive characteristics
0.50	5.382×10^6	2 deg	1:30	Subsonic/Transonic Plume Simulator (PS) + Sting
0.50	5.382×10^6	5 deg	1:30	Subsonic/Transonic PS + Sting
0.95	7.275×10^6	2 deg	1:30	Subsonic/Transonic PS + Sting
0.95	1.765×10^7	2 deg	1:1	Motor-on (MO)
0.95	4.280×10^7	2 deg	1:1	MO
0.95	7.275×10^6	5 deg	1:30	Subsonic/Transonic PS + Sting
0.95	1.765×10^7	5 deg	1:1	MO
0.95	4.280×10^7	5 deg	1:1	MO
1.20	7.108×10^6	2 deg	1:30	Subsonic/Transonic PS + Sting
1.20	7.108×10^6	5 deg	1:30	Subsonic/Transonic PS + Sting
2.01	7.275×10^6	2 deg	1:30	Supersonic PS + Sting
2.01	7.275×10^6	5 deg	1:30	Supersonic PS + Sting
3.02	8.846×10^6	2 deg	1:30	Supersonic PS + Sting
3.02	1.454×10^7	2 deg	1:1	MO
3.02	2.388×10^7	2 deg	1:1	MO
3.02	8.846×10^6	5 deg	1:30	Supersonic PS + Sting
3.02	1.454×10^7	5 deg	1:1	MO
3.02	2.388×10^7	5 deg	1:1	MO

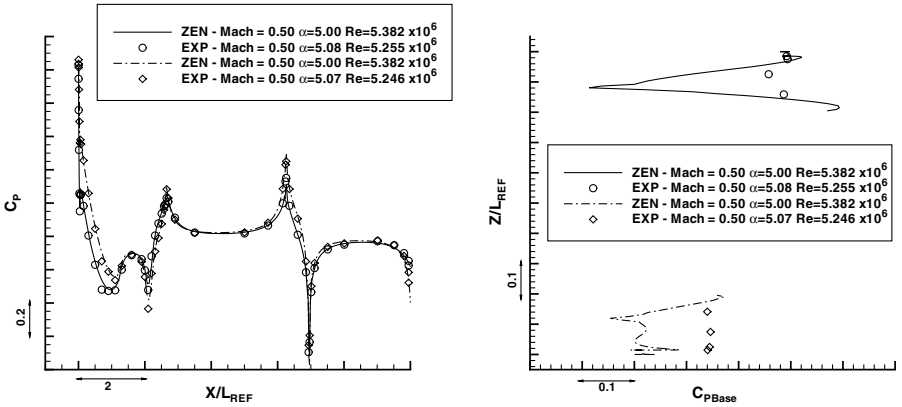

a) Body b) Base

Fig. 8 Pressure distribution in the subsonic regime: (solid line) ∘ lee side; (dashed-dotted line) ⋄ wind side.

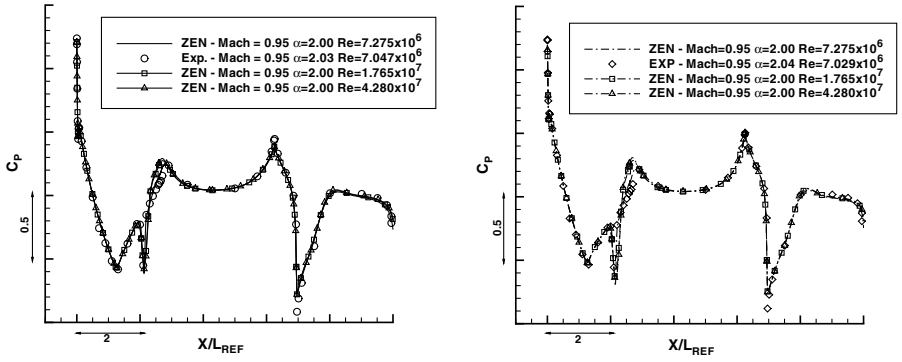

a) Lee side b) Wind side

Fig. 9 Pressure distribution in the transonic regime: no symbol Re_{WT}, □ Re_{INT}, △ Re_{FL}.

Fig. 10) on the wind side with separation lines and detached eddies departing downstream. The flowfield is reproduced satisfactorily by the numerical simulation.

The extension of the separated flow region on the boat-tail decreases as the Mach number increases, and at $M = 1.20$ is just a little zone on the lee side. The pressure coefficients obtained at $M = 1.20$ and at two different angles of attack are shown in Fig. 11. An excellent agreement with the experimental measurements has been achieved. A weak bow shock occurs in front of the launcher's nose. Shocks are present downstream of the boat-tail when the flow realigns on the intermediate cylinder, and at the flare. An analysis of both experimental and numerical flow fields shows that, at $\alpha = 5$ deg, a flow separation with the presence of recirculation regions occurs at the junction between the intermediate cylinder and the flare. Separation lines are present on the flare and I stage indicating a system of detached vortices.

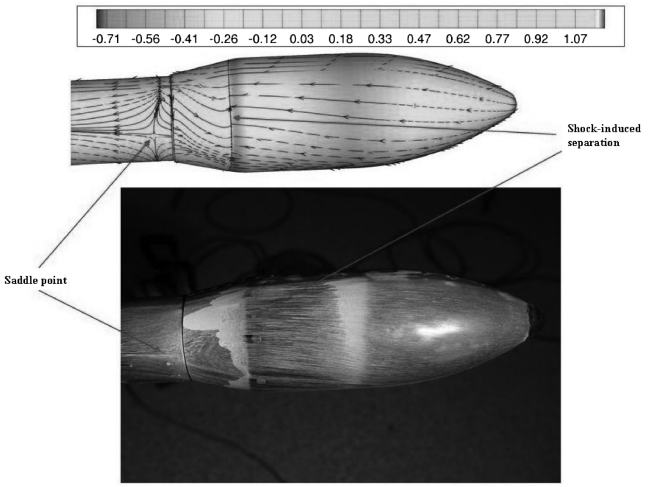

Fig. 10 Transonic flow regime: $M = 0.95$, $\alpha = 5.0$ deg. Comparison between numerical (skin friction lines) and experimental (oil flow visualization) fields. Contour map of pressure coefficient C_P.

The radial pressure distribution computed in the transonic flow regime on the base of the launcher is shown in Figs. 12 and 13. At Mach number 0.95 (left plot of Fig. 12) the effect of the Reynolds number is clearly visible. Experimental data agree better with the results computed at the intermediate and flight Reynolds numbers than with those obtained numerically on the wind tunnel configuration. As a matter of fact, the simulation of the base flow in the transonic, as well as in the subsonic, regime is really critical (right plot of Fig. 12). Recirculation bubbles are present in the region between the base and the nozzle whereas a supersonic zone exists at the exit of the annular nozzle of the plume simulator. A strong shear layer is formed. The Mach number decreases from freestream to very low values in the recirculation regions, and then a sudden and strong expansion occurs where the supersonic jet exits from the annular nozzle. The situation is further complicated by the system of detached eddies that contribute to the unsteadiness of the flow. The zone of interaction of the external stream with the jet plume is quite large, about two times the nozzle length, and a significant suction effect, with a consequent increase of the drag coefficient, is produced.

The left plot of Fig. 13 shows the pressure on the base of the launcher at $M = 1.20$. The situation is not as critical as for Mach number 0.95. The numerical results show some expansion peaks that seem to be not present in the experiments. However, the pressure coefficient is reproduced quite well on average. The zone of interaction between the jet plume and the external stream decreases as the Mach number increases (right plot of Fig. 13) and the prediction of the base flow becomes less critical.

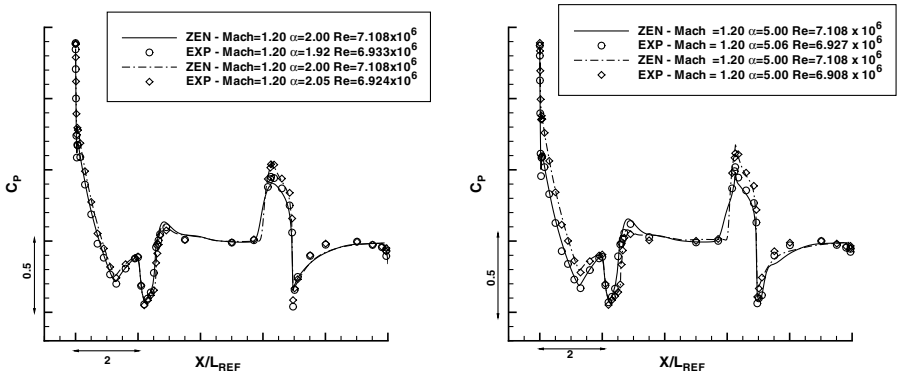

a) $\alpha = 2$ deg **b) $\alpha = 5$ deg**

Fig. 11 Pressure distribution in the transonic regime: Re_{WT}; (solid line) ∘ lee side; (dashed-dotted line) ⋄ wind side.

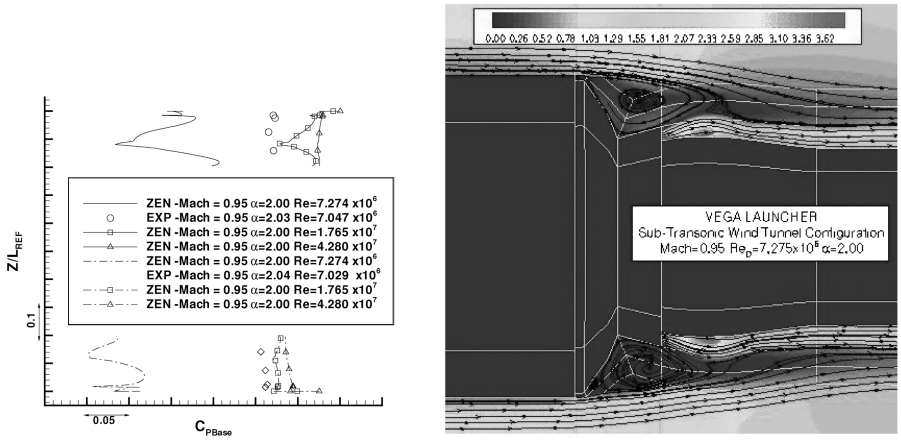

a) Radial pressure distribution : (solid line) ∘ lee side; (dashed-dotted line) ⋄ wind side **b) Mach number distribution and streamlines**

Fig. 12 Base flow in the transonic regime: $M = 0.95$.

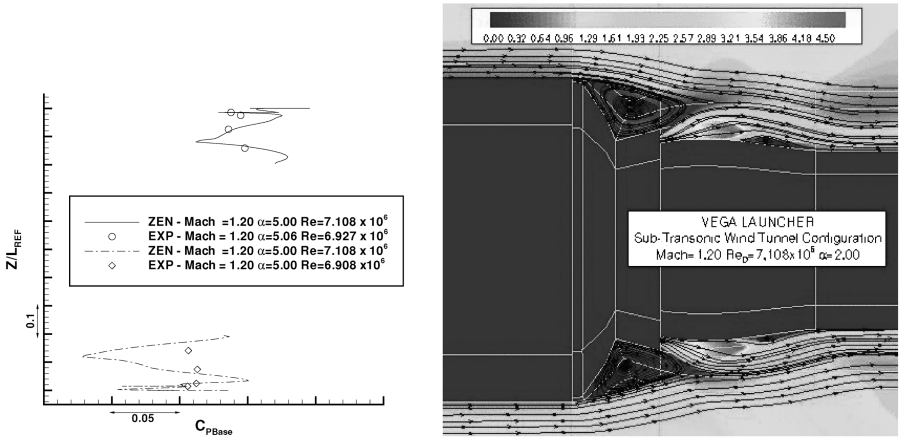

a) Radial pressure distribution : (solid line) ∘ lee side; (dashed-dotted line) ⋄ wind side **b) Mach number distribution and streamlines**

Fig. 13 Base flow in the transonic regime: $M = 1.20$.

C. Supersonic Flow Regime

In the supersonic regime, the flow around the wind tunnel configuration with the plume simulator and sting has been analyzed at Mach number 2.01 and 3.02, at $\alpha = 2$ and 5 deg. The Reynolds number effect has been evaluated at $M = 3.02$.

The computed pressure distributions on the lee and wind side of the launcher are shown in Fig. 14, where also experimental data are plotted showing a good agreement along the launcher's surface. The flow presents a bow shock in front of the nose, and a weak shock between the boat-tail and the intermediate cylinder where the pressure coefficient is nearly flat. A rather strong shock occurs between the intermediate cylinder and the flare. Information on the flow topology can also be derived from the oil flow visualizations taken during the experiments (Fig. 15). A separated region with recirculation zones is visible upstream of the flare on lee side at intermediate angles of attack (left plot of Fig. 15). This foci-type

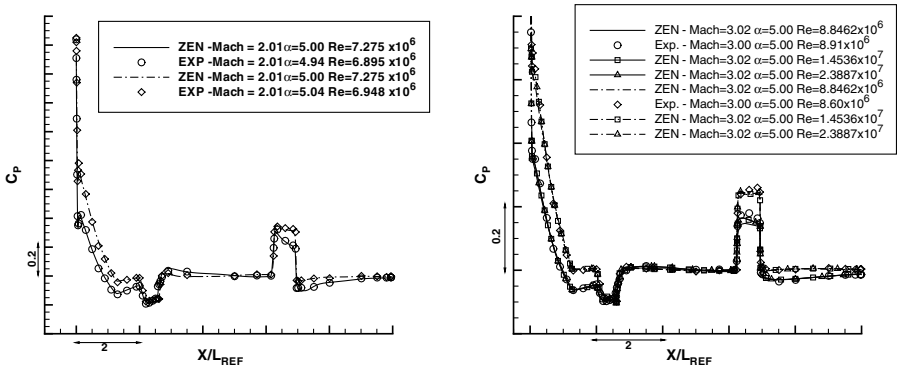

a) $M = 2.01$ b) $M = 3.02$

Fig. 14 Pressure distribution in the supersonic regime: (solid line) ∘ lee side; (dashed-dotted line) ⋄ wind side.

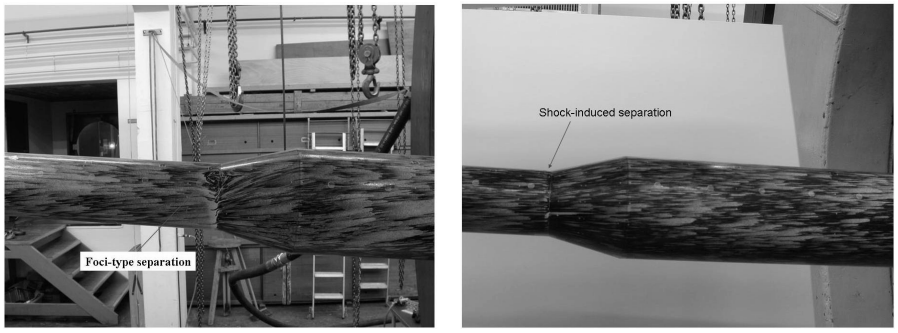

a) $M = 1.58$, $\alpha = 5$ deg b) $M = 2.01$, $\alpha = 2$ deg

Fig. 15 Oil flow visualizations in the supersonic regime.

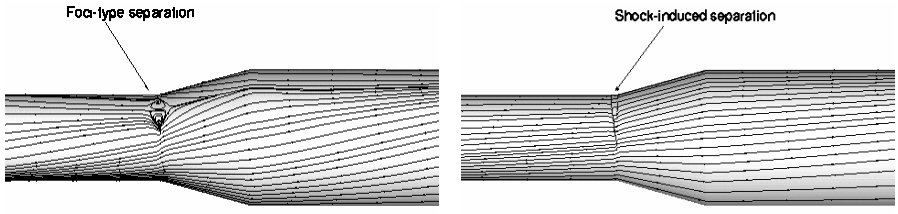

a) $\alpha = 5$ deg b) $\alpha = 2$ deg

Fig. 16 Skin friction lines in the supersonic flow regime: $M = 2.01$.

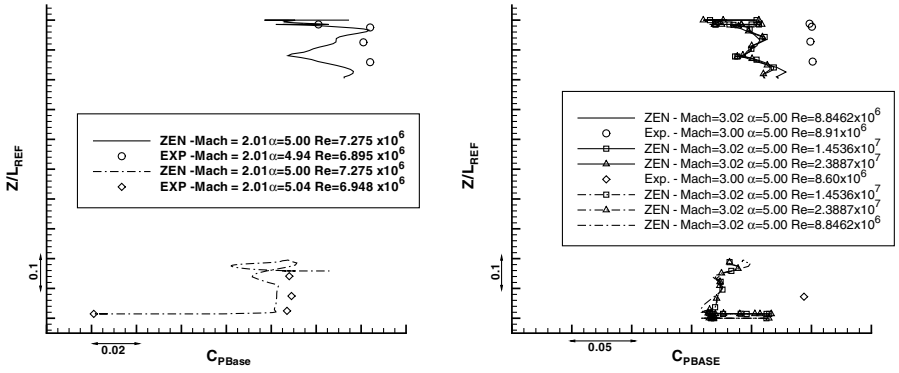

a) $M = 2.01$ b) $M = 3.02$

Fig. 17 Pressure distribution on the base in the supersonic regime: (solid line) ∘ lee side; (dashed-dotted line) ⋄ wind side.

separation, due to the interaction between the vortex field generated on the intermediate cylinder and the shock wave forming upstream of the flare, is typical of the cylinder-flare configurations in supersonic regime at intermediate angles of attack [15]. The recirculation regions disappear at lower incidence (right plot of Fig. 15). The CFD simulations return the same type of flow. The skin friction lines computed at Mach 2.01 are reported in Fig. 16. The foci-type separation is present at $\alpha = 5$ deg on the lee side upstream the flare, whereas a "simple" shock-induced separation is obtained at $\alpha = 2$ deg (the same can be said for Mach 3.02).

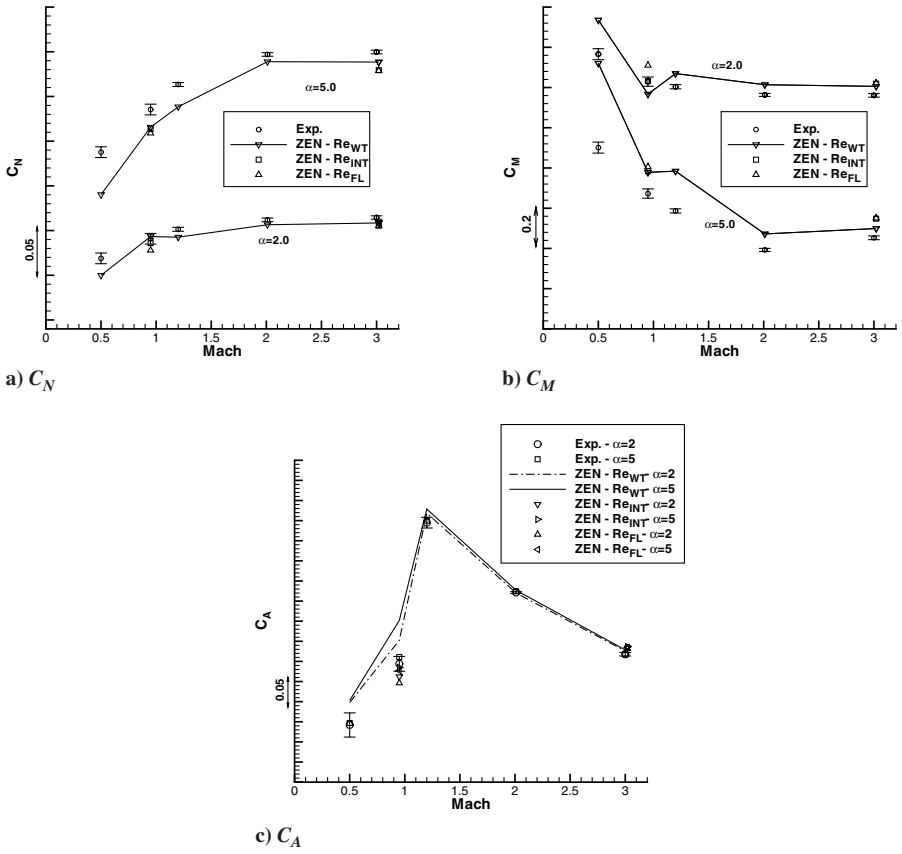

a) C_N b) C_M

c) C_A

Fig. 18 Aerodynamic coefficients.

The pressure distributions computed on the base of the launcher are shown in Fig. 17. At Mach number 2.01 a good agreement with the experimental data has been achieved and expansion peaks are present in both the computed and measured distributions. At Mach number 3.02 no Reynolds number effect is predicted and the "numerical" plume simulator reproduces on the base of the scaled model the same pressure computed for the flight configuration. Even though a discrepancy between the computed and the experimental results is present, such a difference is not important in this case because the contribution of the base to the total drag is not very significant at this Mach number.

D. Aerodynamic Coefficients

Normal, axial force, and pitching moment coefficients are reported in Fig. 18 as functions of the Mach number, at $\alpha = 2$ and 5 deg, at different Reynolds numbers. The normal force coefficient, accordingly to Mach number independence principle, tends to a limit value at both the incidences. The comparison with the measured data is rather good at $\alpha = 2$ deg except at $M = 0.50$ that is, however, affected by unsteady phenomena [13,16]. A systematic underestimation of the numerical data is present at $\alpha = 5$ deg. This is probably due to a wrong quantitative prediction of the system of the eddies detaching on the lee side of the launcher, and of the associated vortex lift. Limited resolution of the grid in the azimuthal direction and location of the far-field boundaries are the possible culprits. The C_N results are weakly influenced by the Reynolds number.

The axial force coefficient strongly depends on the base drag. In subsonic and transonic regimes, where the contribution of the base to the total drag is large, a not completely satisfactory agreement with the experimental data is obtained. In the supersonic regime, instead, the contribution of the base is not significant and a good agreement with the measured axial force coefficients is achieved. The drag rise is present in the transonic flow regime and the maximum of C_A is reached at Mach 1.20 at both the angles of attack. The Reynolds number has an influence on the C_A, but this is only due to the base, as the pressure distributions show.

The pitching moment coefficient has been computed with respect to the nose-tip of the launcher, and decreases with the Mach number becoming constant in the supersonic regime. The comparison between numerical and experimental results follows the normal coefficient curve because $C_M = -C_N X_{\mathrm{CP}}/D$. An oscillation, apparently not measured in the experiments, is present in the transonic CFD data.

The experimental results have been reported in Fig. 18 together with the error bars, larger in the subsonic and transonic than in the supersonic flow regime. The uncertainty of the C_A measured at $M = 0.50$ is quite evident.

E. Contribution to Ground-to-Flight Extrapolation

Laws of extrapolation-to-flight of the global aerodynamic coefficients in the form

$$C_{N,A,M} = a[\log_{10}(Re)]^b \tag{2}$$

with a and b being functions of α and M, have been found. CFD has played an important role [14] in the extrapolation-to-flight procedure adopted [17]. Results at different Reynolds numbers and preliminary trends have been obtained through the numerical simulations. To perform a detailed correlation with the experimental data, the "distributed" aerodynamic coefficients defined as

$$\begin{aligned} C_{N,A}(x) &= \int_0^x \frac{2\pi r(x) C_{n,a}(x)}{S_{\mathrm{REF}}}\,\mathrm{d}x \\ C_M(x) &= \int_0^x \frac{2\pi r(x) C_m(x)}{S_{\mathrm{REF}} D}\,\mathrm{d}x \end{aligned} \tag{3}$$

have been computed by integrating the pressure and friction coefficients along the launcher longitudinal axis. Moreover, the integration has been performed on the parts in which the launcher has been subdivided, as shown in Fig. 1, and the "lumped" coefficients have been obtained. This has allowed to identify the discrepancies between numerical and experimental data, and to understand the

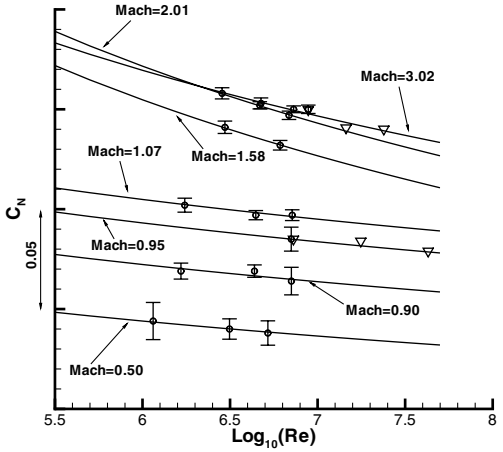

Fig. 19 Normal force coefficient as function of the Reynolds and Mach numbers: Solid line, Eq. (2); ○ experimental data + error bars; ▽ corrected CFD data.

reasons of the differences. In this way the preliminary trends with the Reynolds number have been corrected and the functions of Eq. (2) determined. As an example of the results achieved, the normal force coefficient at $\alpha = 5$ deg as a function of the Reynolds and Mach numbers is reported in Fig. 19.

VII. Conclusions

CIRA has been charged of studying the aerodynamics of the four-stage configuration of the Vega launcher to define reliable laws to extrapolate the aerodynamic coefficients measured in the wind tunnel tests to the actual conditions of the ascent flight path. Numerical simulations, complementary to experimental test campaigns, have been performed using the Reynolds-averaged formulation of the Navier–Stokes equations. The 1:30-scaled model with the plume simulator and sting at the wind tunnel conditions, and the full-scale configuration at the flight Reynolds number have been considered. To study the Reynolds number effects, simulations at an intermediate Reynolds number have also been carried out. The motor-on conditions have been investigated by a boundary condition capable of reproducing the pressure and momentum field at the engine nozzle exit. The results obtained in the subsonic, transonic, and supersonic flow regimes up to Mach number 3.02 have been presented and discussed.

A globally satisfactory agreement with the experimental data over a wide range of flow regimes and Reynolds numbers has been achieved. Pressure distributions have been reproduced in an excellent way over all the launcher with the exception of the base. A proper physical and numerical modeling of the base flow has turned out to be of significant importance in the subsonic and transonic regimes where the contribution of the base to the total drag is large. The effect of this issue on the definition of the extrapolation laws of the aerodynamic coefficients has been addressed by properly analyzing the experimental and numerical data.

The main characteristics of the flow have been well reproduced. In the transonic regime a separation, whose extension decreases as the Mach number increases, is present on the boat-tail. A saddle point with eddies detached downstream occurs on the intermediate cylinder. In the low supersonic regime ($M = 1.20$ and 2.01), a foci-type separation is present on the lee side upstream of the flare at $\alpha = 5$ deg. Eddies are detached on the flare and first stage, whereas at lower incidences and at Mach number 3.02 a simple shock-induced separation occurs at the junction between the intermediate cylinder and the flare. The computed flowfields qualitatively compare well with the experimental visualizations. An under-prediction of the vortex lift has been noted at almost all the Mach numbers investigated. This can be reasonably ascribed to an underestimation of the strength of the lee side vortices.

As a final remark, it is worth pointing out the role that CFD has played in supporting the wind tunnel campaigns and the extrapolation-to-flight procedure. For example, the design of plume simulator system for the subsonic and transonic tests has been modified following the results of a numerical sensitivity study performed during the first phase of the project. Important information to define laws of extrapolation-to-flight of the measured aerodynamic coefficients has been provided by the numerical simulations.

References

[1] Korst, H. H., White, R., and Page, R., "Interference-Free Wind Tunnel Testing of Jet Propelled Missiles," *Aerospace Science and Technology*, Vol. 2, No. 8, 1998, pp. 481–488.

[2] Anon., "Quality Assessment for Wind Tunnel Testing," AGARD AR-304, 1994.

[3] Catalano, P., and Amato, M., "An Evaluation of RANS Turbulence Modelling for Aerodynamic Applications," *Aerospace Science and Technology*, Vol. 7, No. 7, 2003, pp. 493–509.

[4] Catalano, P., and Amato, M., "Assessment of κ-ω Turbulence Modeling in the CIRA Flow Solver ZEN," *Proceedings of ECCOMAS 2001 Conference* [CD-ROM], Institute of Mathematics and Its Applications, Southend-on-Sea, Essex, U.K., 2001.

[5] Amato, M., and Catalano, P., "Non Linear κ-ε Turbulence Modeling for Industrial Applications," *Proceedings of ICAS 2000 Congress*, [CD-ROM], Optimage, Edinburgh, U.K., 2000, Paper 2-7-3.

[6] Kok, J., "Resolving the Dependence on Free-Stream Values for the κ-ω Turbulence Model," *AIAA Journal*, Vol. 38, No. 7, 2000, pp. 1292–1295.

[7] Marongiu, C., Catalano, P., Amato, M., and Iaccarino, G., "U-ZEN: A Computational Tool Solving U-RANS Equations for Industrial Unsteady Applications," AIAA Paper 2004-2345, July 2004.

[8] Anderson, J. D., *Hypersonic and High Temperature Gas Dynamics*, McGraw–Hill, New York, 1989.

[9] Catalano, P., and Vitagliano, P. L., "A Scalable Wall Functions Approach for High Reynolds Number Flows," *Proceedings of First European Conference for Aero-Space Sciences (EUCASS)* [CD-ROM], TsAGI, Moscow, 2005, Paper 2-09-07.

[10] Roache, P. J., *Verification and Validation in Computational Science and Engineering*, Hermosa Publishers, Albuquerque, NM, 1998.

[11] Marini, M., Catalano, P., Roncioni, P., and Di Clemente, M., "Vega Wind Tunnel Test Activity. CFD Analysis for Sensitivity Characterisation," CIRA, S.c.p.A. CIRA-TR-03-497, Capua (CE), Italy, Dec. 2003.

[12] Marini, M., Catalano, P., Roncioni, P., and Di Clemente, M., "Vega Wind Tunnel Test Activity. CFD Analysis for Ground-to-Flight Extrapolation Support," CIRA, S.c.p.A. CIRA-CF-04-0418, Capua (CE), Italy, Jan. 2005.

[13] Nicolí, A., Imperatore, B., Fauci, R., and Pizzicaroli, A., "Wind Tunnel Test Campaigns of the VEGA Launcher," AIAA Paper 2006-0257, Jan. 2006.

[14] Catalano, P., Marini, M., Vitagliano, P. L., and Pizzicaroli, A., "CFD Role in the Extrapolation-to-Flight Procedure of the Vega Launcher Aerodynamic Data-Base," *Proceedings of XVIII Congresso Nazionale AIDAA* [CD-ROM], AIDAA, Rome, 2005.

[15] Rom, J., *High Angle of Attack Aerodynamics, Subsonic Transonic and Supersonic Flow*, Springer–Verlag, New York, 1992.

[16] Romblad, J., "Wind Tunnel Test of a 1:30 Scale Model of the VEGA Launcher in the FOI/FFA Wind Tunnel T1500," FOI, FOI-MEMO-894, Stockholm, June 2004.

[17] Nicolí, A., Imperatore, B., Marini, M., and Catalano, P., "A Ground-to-Flight Extrapolation Procedure for a Launcher Configuration," *Proceedings of First European Conference for Aero-Space Sciences (EUCASS)* [CD-ROM], TsAGI, Moscow, 2005, Paper 2-03-07.

R. Cummings
Associate Editor